Abyssal Mixing in the Brazil Basin*

MICHELE Y. MORRIS

National Institute of Water and Atmospheric Research, Wellington, New Zealand

MELINDA M. HALL,+ LOUIS C. ST. LAURENT,# AND NELSON G. HOGG

Woods Hole Oceanographic Institution, Woods Hole, Massachusetts

(Manuscript received 22 August 2000, in final form 19 April 2001)

ABSTRACT

One of the major objectives of the Deep Basin Experiment, a component of the World Ocean Circulation Experiment, was to quantify the intensity and spatial distribution of deep vertical mixing within the Brazil Basin. In this study, basin-averaged estimates of deep vertical mixing rates are calculated using two independent methodologies and datasets: 1) vertical fluxes are derived from large-scale temperature and density budgets using direct measurements of deep flow through passages connecting the Brazil Basin to surrounding basins and a comprehensive hydrographic dataset within the basin interior and 2) vertical mixing rates are estimated from finescale bathymetry and hydrographic data using a functional relationship between turbulent dissipation and bathymetric roughness, deduced from localized measurements of ocean microstructure obtained during the Deep Basin Experiment. The space–time mean estimates of vertical mixing diffusivities across representative surfaces within the Antarctic Bottom Water layer fell in the range $\overline{\kappa} \sim 1$–$5(\times 10^{-4}\ \mathrm{m^2\ s^{-1}})$ and were indistinguishable from each other within the estimation uncertainties. The mixing rates inferred from potential temperature budgets update, and are consistent with, earlier estimates that were based on less data. Mixing rates inferred from budgets bounded by neutral surfaces are not significantly different from the former. This implies that lateral eddy fluxes along isopycnals are not important in the potential temperature budgets, at least within the large estimation uncertainties. Unresolved processes, such as cabbeling and low frequency variability, which complicate inference of mixing from large-scale budgets, have been considered. The agreement between diffusivity estimates based on a modeled relationship between bathymetric roughness and turbulent dissipation, with those inferred from large-scale budgets, provides independent confirmation that the mixing rates have been accurately quantified.

1. Introduction

The distribution and intensity of diapycnal mixing and vertical velocities in the deep oceans are fundamentally related to the abyssal flow dynamics and stratification. Stommel (1958) was the first to propose a dynamical connection between the abyssal circulation and bottom water formation and modification processes. In his model, cold water sinks in confined, isolated polar regions and travels equatorward in deep western boundary currents, which supply the abyssal ocean interior with cold water that subsequently upwells across the thermocline. The conversion of cold to warm water in this model and many subsequent models of the ocean structure (e.g., Munk 1966) is maintained by downward diffusion of heat via turbulent mixing processes. These vertical mixing processes provide a link between the deep ocean and the surface and so are important elements of the global thermohaline circulation and the earth's climate system. The ability of climate models to simulate the mean state and variability of the ocean–atmosphere system depends critically on accurate parameterization of these processes, so determination of accurate values of the vertical mixing rates is vital.

One of the objectives of the Deep Basin Experiment (DBE), part of the World Ocean Circulation Experiment (WOCE), was to quantify deep diapycnal mixing rates and to provide insight into the relative intensity of boundary and interior mixing (Hogg et al. 1996). A multipronged approach to investigating deep diapycnal mixing was envisaged. Diffusive fluxes would be measured directly from observations of the dispersion of a released tracer, and turbulent transports at small scales would be estimated from ocean microstructure measurements as part of the Brazil Basin Tracer Release

* Woods Hole Oceanographic Institution Contribution Number 10284.

+ Current affiliation: Foundation for Research Science and Technology, Wellington, New Zealand.

Current affiliation: School of Earth and Ocean Sciences, University of Victoria, Victoria, British Columbia, Canada.

Corresponding author's address: Melinda M. Hall, Woods Hole Oceanographic Institution, Mail Stop 21, Woods Hole, MA 02543.
E-mail: mhall@whoi.edu

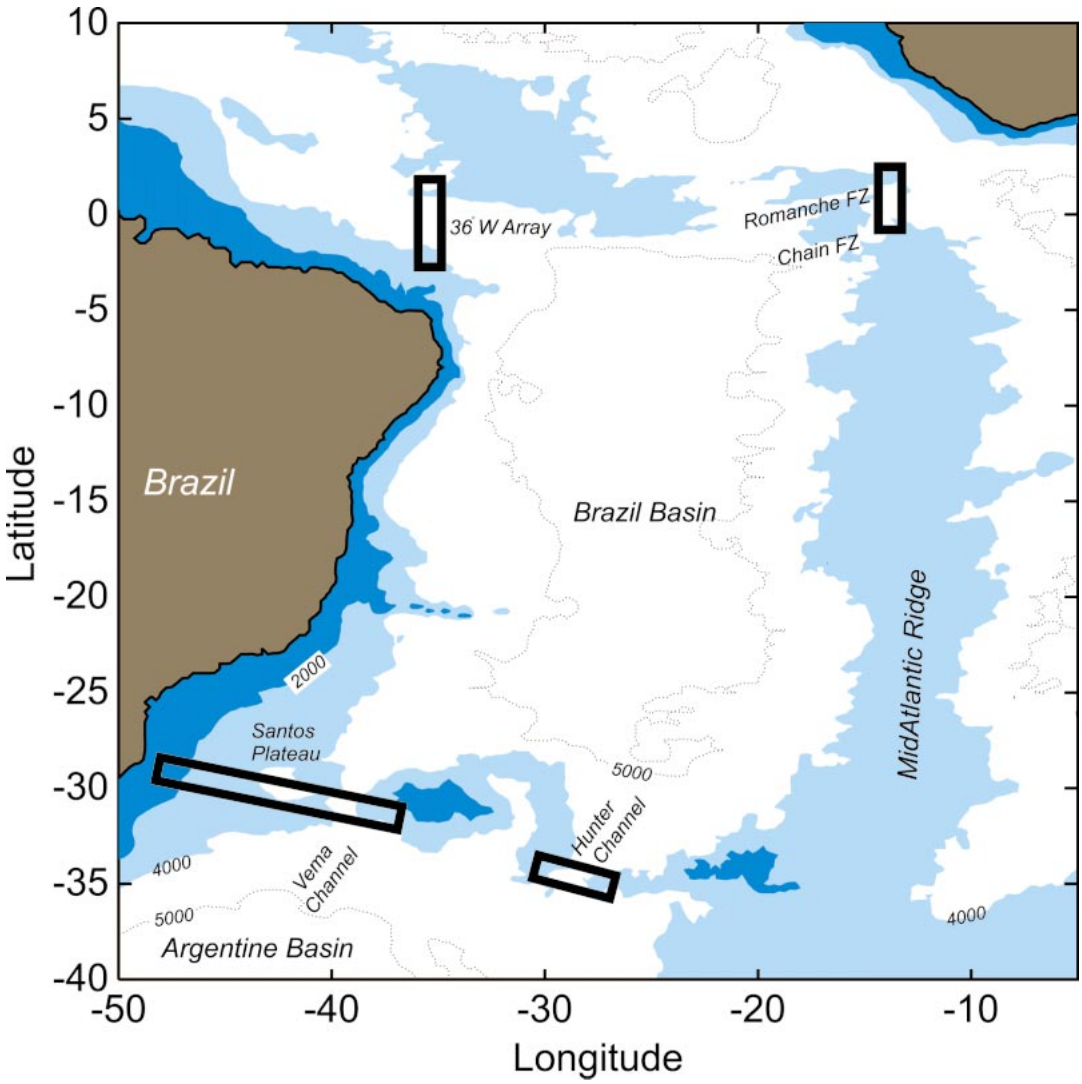

FIG. 1. Setting for the Deep Basin Experiment. The four mooring arrays, deployed in the four channels connecting the Brazil Basin with the surrounding basins, are shown schematically as rectangular boxes. Bathymetry is contoured.

Experiment (Toole et al. 1997a,b; Polzin et al. 1997). These relatively localized estimates of mixing in representative regions of the basin would be complemented by larger-scale estimates inferred from heat and mass budget considerations. The relatively small area and simple geometry of the Brazil Basin, shown in Fig. 1, are well suited for this purpose. There are a limited number of deep passages connecting this basin to others so that it is feasible to monitor the total transport of bottom water into the basin directly. It is also practical to subdivide the basin into smaller enclosed regions using hydrographic sections.

Antarctic Bottom Water (AABW), defined here as water that has a potential temperature θ colder than 2°C, follows a generally northward path through the Brazil Basin (e.g., Reid 1989; Stramma and England 1999), entering and exiting through deep topographic passages. The densest water flowing into the basin through the Vema and Hunter Channels has no deep outlet, and the isotherms defining the upper extent of this water type intersect the seafloor within the basin. The northward increase in the temperature of the water flowing close to the bottom is illustrated in the bottom potential temperature map shown in Fig. 2. An upward flow of water across these deep isothermal (and isopycnal) surfaces is required if the volumes bounded by the surfaces remain constant. The associated conversion of cold to warmer water is believed to be maintained in a steady-state balance by downward diffusion of heat. (Geothermal heating at the ocean floor is negligible in this basin.)

Abyssal upwelling rates in the Brazil Basin have previously been inferred from measurements of the net inflow of dense water by Hogg et al. (1982), leading to

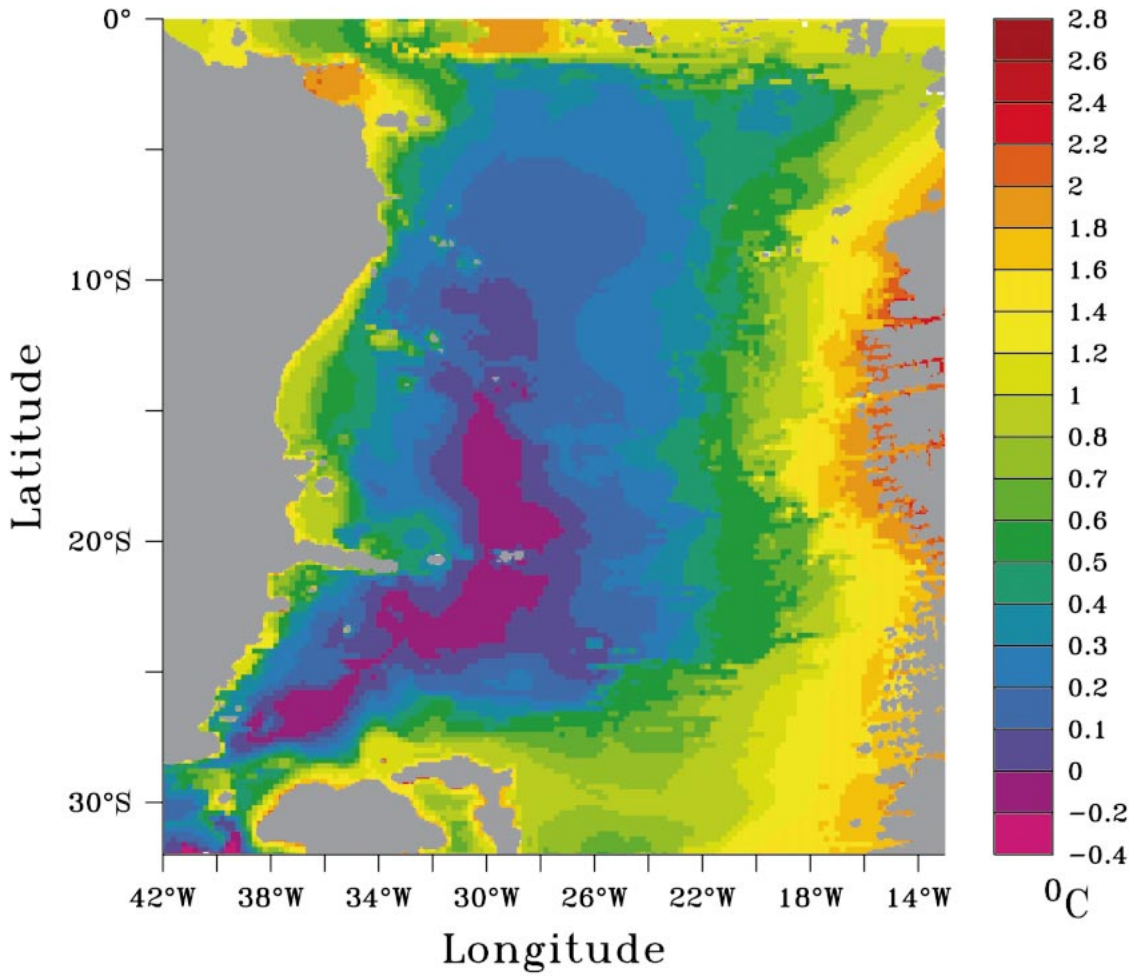

FIG. 2. Potential temperature at the seafloor, showing the northward warming of Antarctic Bottom Water as it flows toward the equator in the Brazil Basin. This climatology was compiled from all available, high quality CTD casts, including recent WOCE data. The mapping technique favors smoothing along isobaths: see discussion in the text.

spatially averaged estimates of the turbulent diapycnal fluxes and vertical eddy diffusivities $\overline{\kappa} = O(10^{-4})$ m^2 s^{-1}. Mixing rates of this magnitude are typical for the ocean interior, when turbulent transports are determined from large-scale advective budgets or by model fitting of observed property distributions (e.g., Munk 1966; Whitehead and Worthington 1982). However, the turbulent fluxes are an order of magnitude higher than local estimates obtained from ocean microstructure profiles collected over the central Brazil Basin (Polzin et al. 1997). Recent results from the Brazil Basin Tracer Release Experiment offer a possible explanation for the seeming disagreement between weak interior dissipation measurements and higher turbulent fluxes deduced from basin-averaged budgets (Ledwell et al. 2000; Toole et al. 1997a,b). Ledwell et al. (2000) report tracer dispersion and turbulent energy dissipation measurements that show significantly enhanced mixing over regions of rough bathymetry, possibly sufficiently intense and distributed over a wide enough region to balance the Hogg et al. (1982) mixing estimates.

Spatial inhomogeneity of mixing rates is not the only issue that complicates comparison of vertical diffusivity estimates from microstructure data with those deduced from basin-scale budgets. Davis (1994) examined the simplified equations that are used to deduce mixing rates from large-scale budgets and found several possible causes of disagreement, including lateral mixing. Lateral mixing of heat along isopycnals may be misinterpreted as a vertical heat flux, if large-scale budgets are calculated over a volume bounded by an isothermal surface and the seafloor, and isopycnals intersect the isothermal surface. This would lead to an erroneously large value of vertical mixing. Thermodynamic mixing effects associated with nonlinearities in the equation of state for seawater also need to be carefully considered within the large-scale budget framework. Effects such as cabbeling and thermobaricity have been shown to produce

water mass transformation, but are not associated with turbulent fluxes (Davis 1994; McDougall 1987).

The extensive high quality datasets collected during the Deep Basin Experiment motivate us to revisit the abyssal mixing calculation of Hogg et al. (1982). The possibility of reconciliation between diffusivity estimates based on tracer dispersion and microstructure, with those deduced from large-scale budgets, provides further justification (Ledwell et al. 2000). The main aim of this paper is to provide the best possible estimate of vertical mixing within the AABW layer in the Brazil Basin from large-scale budget considerations, while addressing possible complicating effects. In particular, we will address the issues of whether lateral mixing has confused previous estimates of diapycnal diffusion and whether neglected terms in the budget equations used to infer diffusivities are important. Second, we will attempt to reconcile these revised estimates with independent basin-averaged diffusivity estimates, which extrapolate the results of the Brazil Basin Tracer Release Experiment to the entire Brazil Basin, using a model of diffusivity dependent on bathymetric parameters.

2. Data and methodology

a. Mixing rates inferred from heat budgets

The vertical diffusivity coefficient κ is inferred following the method of Hogg et al. (1982) and Whitehead and Worthington (1982), using the following steady-state heat balance:

$$\int_V \nabla \cdot (\mathbf{u}\theta)\, dV = \int_V (\kappa\theta_z)_z\, dV, \tag{1}$$

where V is a volume bounded at the top and bottom by isothermal surfaces or the ocean floor, and $\mathbf{u}$ is the three-dimensional flow field. This equation can be rewritten as

$$\int_A \mathbf{u}\theta \cdot \mathbf{n}\, dA = [\overline{\kappa\theta_z} A]_{\text{top}} - [\overline{\kappa\theta_z} A]_{\text{bottom}}, \tag{2}$$

where A refers to the surface area of volume V, with normal vector $\mathbf{n}$, and the overbar indicates an areal average. Diffusive fluxes $\overline{\kappa\theta_z}$ are further approximated as $\overline{\kappa}\,\overline{\theta_z}$. Advective fluxes appearing on the left hand side of (1) are a combination of horizontal fluxes through deep passages around the basin perimeter and nearly vertical fluxes through the top and bottom interfaces. Vertical velocities are obtained from mass conservation. Mixing rates at four representative isotherms, $\theta = 0°$, 0.8°, 1.2°, and 1.6°C, are computed to explore the vertical structure of mixing within the Antarctic Bottom Water layer.

1) PROPERTY DISTRIBUTIONS

A hydrographic climatology was compiled for the purpose of this analysis using all available full-depth CTD (conductivity–temperature–depth) data. Over half the stations shown in Fig. 3 were occupied between 1991 and 1995, during the WOCE Deep Basin Experiment, as part of an international effort involving groups from France, Germany, the United Kingdom, and the United States. These data are all close to the WOCE Hydrographic Program standards, with accuracies better than 0.002°C in temperature and 0.003 in salinity. (Details on data processing and quality control may be found online at http://oceanic.cms.udel.edu/woce.) The remaining stations were obtained from an historical database and have been quality controlled using criteria described by Curry (1996). Bottle data are excluded, as fine vertical resolution is required for the various property maps. All CTD profiles were bin-averaged into 20-m depth bins.

Maps showing the distribution of various hydrographic properties on specified surfaces were required for our mixing rate calculations. For instance, potential temperature at the seafloor (Fig. 2) was used to determine the surface area A of a volume bounded by the ocean bottom and a given isothermal surface. Property maps were obtained from objective analysis of the CTD data. The mapping stategy was the same in all cases.

First, the property data θ_i from each cast were interpolated to the isothermal, neutral density (γ), or pressure surface of interest, giving $\theta_i(\mathbf{x}_i)$, where $\mathbf{x}_i = (x_i, y_i)$ on the surface of interest. In the case where properties were to be mapped along the ocean bottom, the deepest records of the full-depth casts were the data to be mapped. The mapping was then performed in two stages: first, a spatially dependent large-scale mean was estimated and subtracted from the data at each cast location; then the spatial anomalies were objectively mapped. The large-scale mean estimate $\overline{\theta(\mathbf{a})}$ at location $\mathbf{a} = (x_a, y_a)$ on the surface was a weighted average of the data $\theta_i(\mathbf{x}_i)$, where the weighting w_i depended on spatial separation $\mathbf{a} - \mathbf{x}_i$, that is,

$$\overline{\theta(\mathbf{a})} = \frac{\sum_i w_i \theta_i(\mathbf{x}_i)}{\sum_i w_i}, \tag{3}$$

$$w_i = \exp\left(\frac{|\mathbf{a} - \mathbf{x}_i|^2}{\alpha_l^2}\right), \tag{4}$$

and α_l, the length scale for the broad-scale field, was chosen to be large (400 km) to represent the smoothed field.

The next step involved mapping the spatial anomalies from this large-scale mean. The maps required information about the statistics of the field to be mapped, as well as the noise terms. The signal in our case was the long-term mean of the property to be mapped. Sampling errors, due to irregular spatial distribution (see Fig. 3) and temporal aliasing, contributed the greatest source of uncertainty to our estimate. The mapping method exploited the fact that in the absence of significant forc-

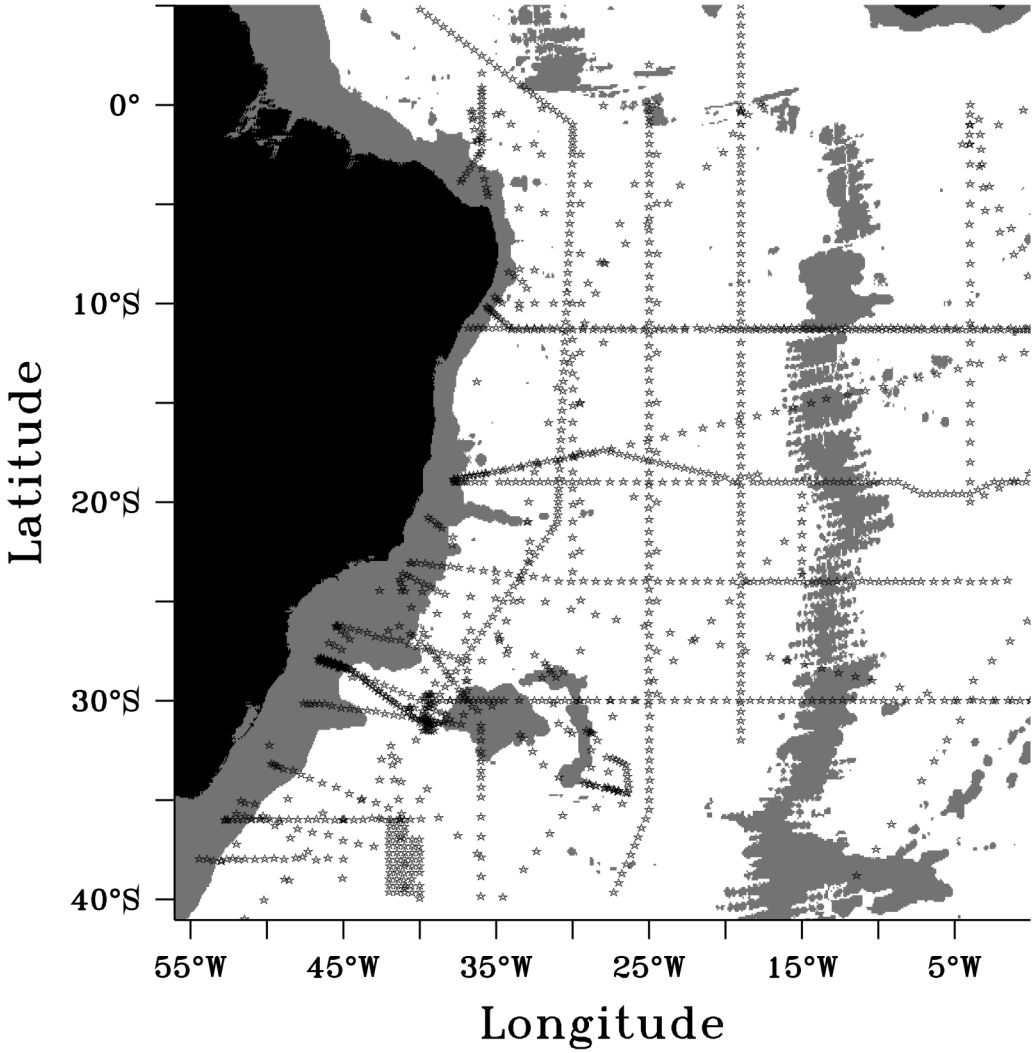

FIG. 3. Location of full-depth CTD stations used in this analysis. Many of the stations were occupied as part of the WOCE Deep Basin Experiment between 1991 and 1995; the rest are from the historical database.

ing, friction, or nonlinear effects, steady barotropic flows are dynamically constrained to follow contours of constant potential vorticity f/H, so one might expect deep property distributions to be preferentially aligned along the same contours. This anisotropy can be incorporated into the estimate by appropriate choice of covariance function (see, e.g., Davis 1998). We chose the data–data covariance function to be Gaussian and a function of the generalized distance R^2,

$$R^2 = \frac{|\mathbf{a} - \mathbf{x}_i|^2}{\alpha_s^2} + \frac{|H(\mathbf{a}) - H(\mathbf{x}_i)|^2}{\lambda^2}, \qquad (5)$$

where $\mathbf{a} - \mathbf{x}_i$ is the spatial separation, α_s is the spatial length scale for the small-scale anomalies, $H(\mathbf{a})$ is the bottom depth at location $\mathbf{a}$, and λ determines the relative contribution of smoothing along isobaths. Bathymetry data at station and estimation grid locations were extracted from the ETOPO5 5-min dataset. The noise covariance was assumed to be diagonal, with a noise-to-signal variance ratio of 0.1, and the data variance was used to set the level of the signal variance.

The challenging aspect of this particular mapping problem was to produce continuous mapped features along tight convoluted bathymetry as well as within the relatively smooth basin interior. We experimented with different mapping parameters by setting α_s at 300 km and varying λ and the signal-to-noise ratio. Increasing λ had the effect of reducing the map's sensitivity to bathymetry, and thus blurred out features around convoluted topography. Reducing the signal-to-noise ratio smoothed the map and decreased the signal amplitude. Both effects resulted in unrealistic map features, such as very cold bottom water spreading to unphysically shallow levels. A choice of 300 km for α_s, 500 m for λ, and 0.1 for the signal-to-noise ratio resulted in maps that interpolated across data-poor regions most suc-

TABLE 1. Properties required for heat budgets over volumes enclosed by four different θ surfaces. The areas enclosed by the contours that delineate the intersection of each θ surface with the sea floor are given in the second column, and their associated errors are in the third column. The vertical gradients of potential temperature averaged across each surface, $\overline{\theta_z}$, are listed in the fourth column; associated errors are in the last column. All properties are derived from objective maps of hydrographic data, as discussed in the text.

θ (°C)	Surface area ($\times 10^{11}$ m^2)	Error (%)	$\overline{\theta_z}$ ($\times 10^{-3}$ °C m^{-1})	Error (%)
1.6	80	8	2.2	16
1.2	71	16	2.1	18
0.8	56	18	1.7	18
0	4.5	35	1.3	27

cessfully, without excessive smoothing. Even so, the smoothing in the mapping has obscured the small tongue of cold water with $\theta < 0$°C from the bottom potential temperature map (Fig. 2), although in the raw data it is evident flowing through the Vema Channel from the Argentine Basin to the Brazil Basin.

The areas subtended by bounding isotherms are calculated from the map of bottom potential temperature shown in Fig. 2 and tabulated along with estimation errors in Table 1. The spatial extent of the $\theta = 0$°C surface is the most sensitive to mapping parameters because spatial gradients of θ over this surface are weak. A potentially large source of error results from temporal changes in bottom water temperatures. These are possibly associated with long-term trends in bottom water properties that have been observed at the deep passages connecting the Brazil Basin to surrounding basins (Hogg and Zenk 1997; Hall et al. 1997; Zenk et al. 1999). This error term is difficult to estimate as repeat hydrographic observations within the basin interior are rare. Investigation showed no evidence of coherent basinwide changes of bottom properties or changes in layer volumes based on this hydrographic dataset. For instance, we observe large-scale changes in θ of about 0.02°C over a decade, on density surfaces within the AABW layer, from repeat occupations at 12°S and 18°S. However the trend was toward warmer, saltier conditions at 12°S, whereas there was a freshening and cooling at 18°S. The approach taken here was to consider a reasonable range of assumed signal-to-noise ratios and mapping scales, and consider the effect on the area computation. These sensitivity studies provide the estimation errors in Table 1.

Vertical gradients of potential temperature at the depth of each bounding isotherm are computed from bin-averaged individual profiles, using centered finite differences in the vertical. The individual gradient estimates are then mapped onto the isothermal surface. Surface-averaged values of θ_z over the bounding isothermal surfaces are tabulated along with their errors in Table 1.

2) TRANSPORTS

As part of the DBE, four moored current/temperature arrays were deployed at the four passages allowing flows of AABW into or out of the Brazil Basin. The various passages are labeled on Fig. 1. In the south, AABW enters through the Vema (4.0 Sv) (Sv $\equiv 10^6$ m^3 s^{-1}) and Hunter (2.9 Sv) Channels; at the northern end of the basin, some exits the basin into the western North Atlantic through a zonal equatorial passage near 36°W (2.0 Sv), and some (1.2 Sv) exits eastward through the Romanche and Chain Fracture Zones (hereafter RFZ/CFZ) into the eastern equatorial Atlantic. Here, AABW transports are calculated over the volume of water bounded by the ocean floor and an upper surface nominally at 2°C. The depth of the 2°C surface along a meridional section from the western side of the Brazil Basin is shown in Fig. 4. The station locations and full-depth sections can be found in the paper by Memery et al. (2000), where these data were first presented. Results from each of the moored arrays have been discussed in detail by the investigators responsible for them: the reader is referred to Hogg et al. (1999) for the Vema Channel, Zenk et al. (1999) for the Hunter Channel, Hall et al. (1997) for the 36°W passage, and Mercier and Speer (1998) for the RFZ/CFZ array.

Three of the arrays have significant overlap in time, having been deployed in fall of 1992 and recovered in late May (Hunter Channel, 36°W) or fall (RFZ/CFZ) of 1994. The Vema Channel array was in the water approximately two years earlier than the remaining arrays. In support of each of the arrays, some CTD data were collected: in most cases, these were used as a guide in converting time series of temperature into potential temperature θ and (in the present work) to determine the relationship between θ and neutral density for each location (see section 2b). For the Hunter and Vema Channels, such data were also used for geostrophic velocity calculations to compare with the directly measured velocities; see individual references.

Evaluation of the left-hand side of (2) requires knowledge of both the mass transport and the temperature flux through each of the passages in particular temperature classes. For the purposes of our calculations, each of the four locations was dealt with somewhat differently, depending on the data product readily available. The southern boundary section is a little different than the other passages as a large part of it is outside the Vema Channel and over the Santos Plateau, where the moored array is too sparse to determine the transports. Thus the current meter data have been used to reference hydrographic sections (mainly a section known as M15 = *Meteor* 15) that span the entire width, by a least squares fit to current meter velocities normal to the section. For the Hunter Channel, mass fluxes were estimated from Fig. 14 of Zenk et al. (1999), which shows AABW transports split into 0.2°C potential temperature classes;

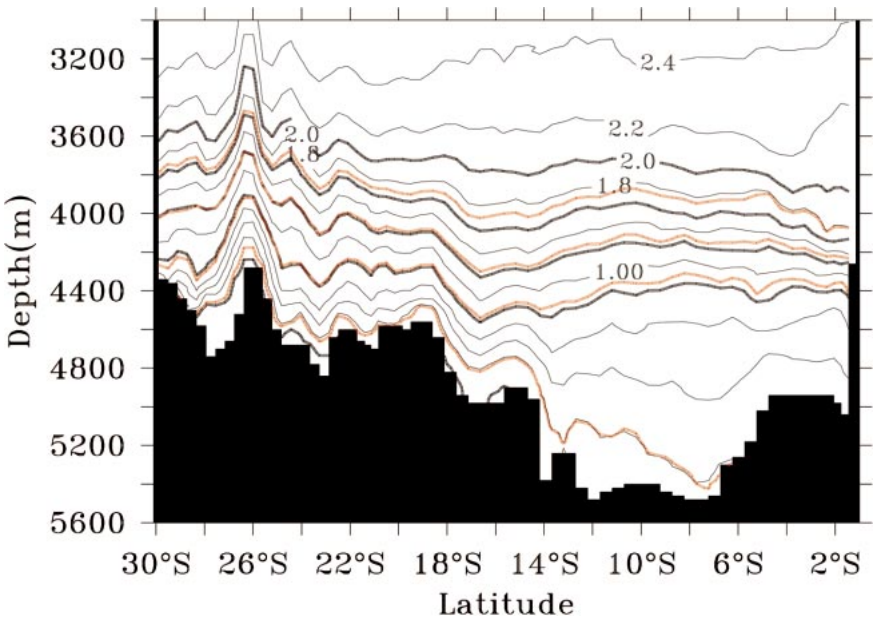

FIG. 4. A vertical section showing potential temperature below 3000 m, along a meridional section from the western part of the Brazil Basin. The section follows the coastline and is located at ~30°W over the northern half of the basin. The contour interval is 0.2°C and five θ surfaces, θ = 0°, 0.8°, 1.2°, 1.6°, 2°C, are shown as heavy lines. Four neutral density surfaces, γ = 28.27, 28.205, 28.16, 28.133 kg m^{-3}, are also shown as red lines. The γ surfaces coincide with the four coldest, highlighted θ surfaces in the Vema Channel, but diverge from θ surfaces in the interior of the Brazil Basin. Full-depth sections and further information can be found in the work of Memery et al. (2000).

θ fluxes were taken to be the midpoint θ of the class times the transport.

At the equatorial boundary, the full velocity and temperature datasets at 36°W were used to calculate the mass and temperature fluxes. For the RFZ/CFZ, H. Mercier generously provided us with time series of array transport and temperature in 5-m depth bins for both locations, from which we could directly calculate the necessary fluxes. In the fracture zones, temperature and velocity were interpolated primarily linearly (but see Mercier and Speer 1998, for details on how data were extrapolated to points where some instruments failed). However, at the 36°W location, the temperature profile in the deep and bottom water has a three-part piecewise linear structure, so strictly linear interpolation between temperatures measured by the moored instruments (at 3900, 4100, and 4300 m) leads to underestimating transports by as much as 40% for the layer $\theta \leq 0.8$°C. Instead, a more complicated, iterative scheme was developed, based on the 22 CTD profiles collected during deployment and recovery, to predict a daily three-part temperature profile in the deep and bottom water from the time series, and this was used to calculate fluxes in the temperature classes (see appendix A).

In section 2b we consider the analogous computation in density space. We note here that for all the locations there is a tight, but latitudinally varying, linear relationship between potential temperature and neutral density in the AABW. This linear dependence of γ on θ, in general, makes the computation of mass and density fluxes in density classes relatively straightforward, once the fluxes for the temperature classes have been determined. Mass and temperature fluxes for four volumes (variously capped by the 0°, 0.8°, 1.2°, and 1.6°C isotherms) are summarized in the schematics of Figs. 5–8, along with errors.

3) TRANSPORT ERRORS

Errors in the heat flux calculations are due both to errors in the estimates of mass transport and to errors from interpolation of temperature in the vertical. The left-hand side of (2) can be rewritten as

$$\sum_{i=1}^{4} M_i\theta_i + M_{\text{upw}}\theta_0 = \sum_{i=1}^{4} M_i\delta\theta_i, \qquad (6)$$

where M_i are the (horizontal) transports (positive leaving the basin) with errors $\sigma(M_i)$, θ_i are transport-weighted average temperatures with errors $\sigma(\theta_i)$, $M_{\text{upw}} = -\Sigma_{i=1}^{4} M_i$ by mass conservation, $\delta\theta_i = \theta_i - \theta_0$, and θ_0 is the temperature of the upper surface. The total error for the heat divergence h is

$$\sigma(h) = \left\{\sum_{i=1}^{4} ([\sigma(M_i)\delta\theta_i]^2 + [\sigma(\theta_i)M_i]^2)\right\}^{1/2}, \qquad (7)$$

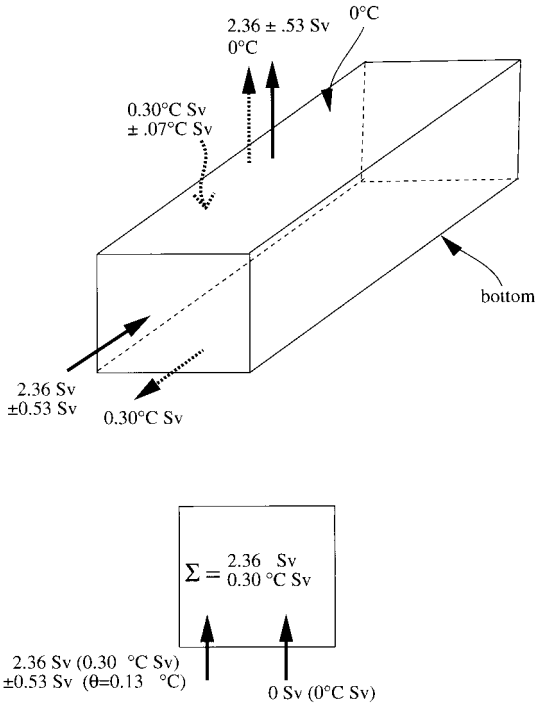

FIG. 5. Diffusive heat flux inferred at the $\theta = 0°C$ isotherm. Bottom: Measured advective fluxes, through the four main channels at the basin perimeter, are shown schematically; moving anticlockwise from the bottom left corner are the transports at the Vema Channel, Hunter Channel, Romanche/Chain Fracture Zones and the equatorial passage at 36°W, respectively. Volume transports are shown with errors. Temperature fluxes and transport-weighted temperatures are shown in parentheses. (Only two decimal places are shown: in some cases, rounding errors may lead to apparent inconsistencies between the fluxes and the transport-weighted temperatures.) Volume and temperature fluxes summed over all four channels are given in the center of the box (convergences are negative). Top figure: Results of the heat budget. Advective mass transports [observed through the passages (front of box) and inferred at the bounding interface (top of box)] are shown as solid lines, temperature transports as dashed. Curved arrows give the inferred diffusive temperature transports.

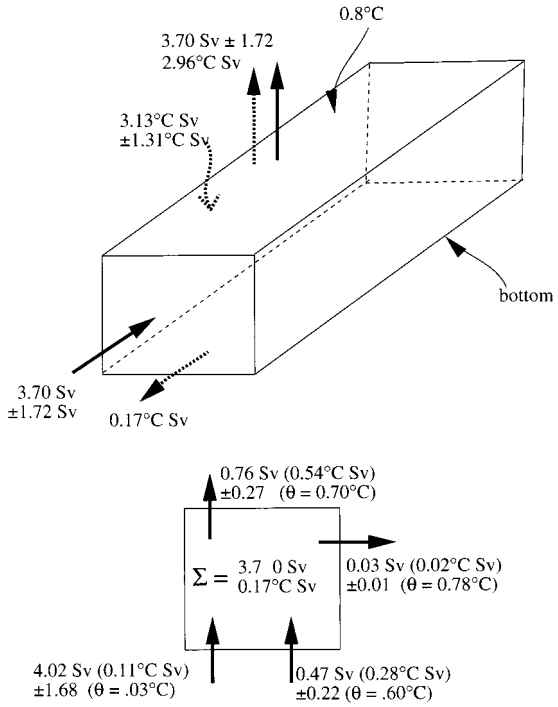

FIG. 6. As in Fig. 5 except the bounding interface is $\theta = 0.8°C$.

assuming that the mass and temperature errors are independent and that errors between different passages are uncorrelated. In fact, there is some temporal coherence between velocities and temperatures, but it is difficult to estimate an average effect for the integrated mass transports, over all locations. Instead we caution that the errors presented should be considered a lower bound. The transport-weighted temperatures are similar to the spatially averaged values, so for $\sigma(\theta_i)$ we use the error associated with interpolating temperature profiles vertically (see appendix A). From appendix A, $\sigma(\theta_i) = 0.04°C$ for all locations, except the Vema Channel, where hydrographic data are used to calculate the fluxes; here all the error gets folded into the mass flux error.

The mass transport errors comprise both temporal and spatial errors associated with the limited sampling of the velocity field in time as well as space. The former is calculated in most cases as a standard error of the mean, where the number of degrees of freedom is the record length of the series divided by twice the integral time scale. Spatial sampling errors arise from several sources and are harder to estimate. The references noted above contain thorough discussions of these errors, and

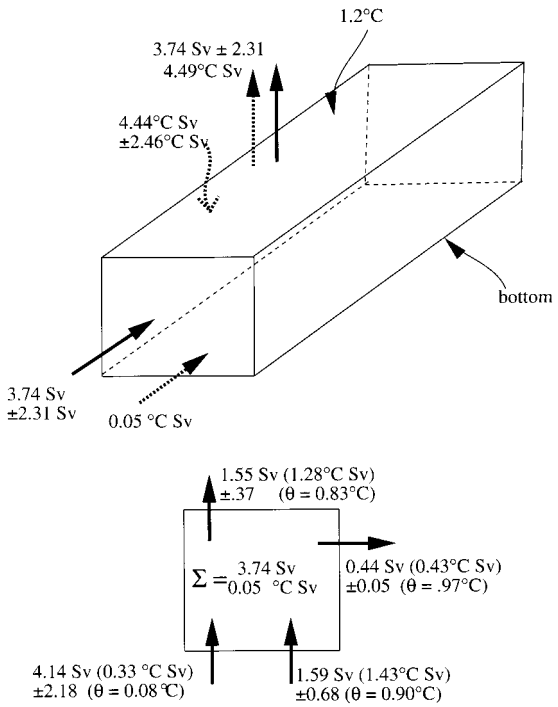

FIG. 7. As in Fig. 5 except the bounding interface is $\theta = 1.2°C$.

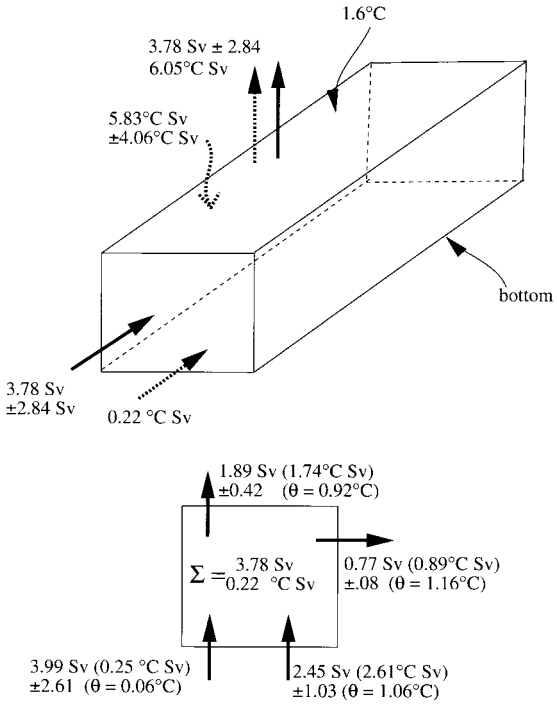

FIG. 8. As in Fig. 5 except the bounding interface is $\theta = 1.6$°C.

these have been adapted for the various layers considered here (see appendix B for details). The total error incurred in the calculation of κ, the diffusion coefficient, is due to the errors in estimating the area of the surface considered, the vertical gradient of θ (or γ) on that surface, and the downward diffusion of heat inferred from the mass and temperature fluxes, the first two of which were discussed in a previous section.

The total error due to advection (see Figs. 5–8) tends to be dominated by the contribution from the Vema Channel. Notice that in the deep layers, the transport error is similar to that in the area and vertical temperature gradient percentage-wise, but as we move upward to shallower surfaces, the transport error increasingly dominates the total. Furthermore, error contributions from the southern boundary dominate over those from the equator, where the flow is either more confined (as in the RFZ/CFZ arrays) or has a simpler spatial structure.

b. Density coordinates

An alternate estimate of κ is obtained if density, rather than potential temperature, is considered. The same steady-state tracer balance as in (2) is used but with θ replaced by neutral density γ. In this coordinate system, the contribution from lateral eddy fluxes is minimized as the bounding surfaces are neutral surfaces. Thus one would expect a reduction of turbulent transport (and κ) if lateral mixing contributed significantly to the heat budget calculated in θ coordinates.

TABLE 2. Properties required for neutral density budgets over four different neutral density surfaces. As for Table 1, the surface areas and averaged vertical gradients of neutral density, $\overline{\gamma_z}$, are derived from objectively mapped hydrographic data.

γ (kg m^{-3})	Surface area ($\times 10^{11}$ m^2)	Error (%)	$\overline{\gamma_z}$ ($\times 10^{-4}$ kg m^{-4})	Error (%)
28.133	79	9	−1.7	13
28.160	72	12	−2.1	12
28.205	62	15	−1.6	13
28.270	23	32	−1.1	20

Neutral density profiles have been calculated using CSIRO software (Jackett and McDougall 1997). The spatial extent of γ surfaces obtained from maps of γ close to the seafloor (not shown), along with area-averaged values of the vertical gradient γ_z, are tabulated in Table 2 for four neutral density surfaces: $\gamma = 28.27$, 28.205, 28.16, and 28.133 kg m^{-3}. These γ surfaces have been chosen to coincide with the $\theta = 0°$, 0.8°, 1.2°, and 1.6°C surfaces at the Vema Channel, but later diverge across the Brazil Basin, lying some 0.2°C warmer at the equator (see for example, Fig. 4). The largest divergence occurs between the coldest θ and densest γ layer; the spatial extent of the $\gamma = 28.27$ surface is five times that of the coldest potential temperature surface and may lie up to 150 m above the deeper surface. We remark here that this will make comparison of surface-averaged diffusion rates somewhat ambiguous for the densest surface, as differences in $\overline{\kappa}$ calculated using heat and density budgets may be caused by isopycnal mixing effects or they may reflect horizontal and vertical variability in diffusive mixing. The more buoyant AABW θ and γ surfaces coincide more closely, and angles between the θ and γ surfaces are quite small for these shallower layers.

c. Mixing inferred from bathymetric roughness

Results from the Brazil Basin Tracer Release Experiment suggest that diapycnal mixing in the deep Brazil Basin is strongly enhanced in regions of rough bathymetry (Polzin et al. 1997; Toole et al. 1997a,b; Ledwell et al. 2000; St. Laurent et al. 2001). Observations of both tracer dispersion and microstructure derived mixing rates indicate that turbulent diffusivities exceed $\kappa = (2 - 4) \times 10^{-4}$ m^2 s^{-1} in a region near the Mid-Atlantic Ridge (MAR). In fact, Ledwell et al. (2000) and St. Laurent et al. (2001) report dissipation estimates that imply diffusivities between 10 and 30 ($\times 10^{-4}$ m^2 s^{-1}) for the dense water along the sloping walls of abyssal fracture zones (FZs). We hypothesize that such large diffusivities are characteristic of rough topography throughout the basin. While a large extent of the basin's area is characterized by the rough topography of the MAR and its associated FZs, these features are absent over broad regions of the western half of the basin, from where Polzin et al. (1997) analyzed a sparse number of

dissipation profiles and found no enhancement of mixing rates. However, steep slopes are found in the western basin along the continental rise, and the Vitoria–Trindade Seamount Chain, which extends from the continental margin into the basin's interior. The extent to which mixing rates are enhanced over steep topographic features of the western basin such as these has not been established, but enhanced mixing rates have been observed over seamounts at other sites (Toole et al. 1997a,b; Lueck and Mudge 1997).

While measurements of mixing rates from the Brazil Basin are sparse, the observations of Polzin et al. (1997) suggest that abyssal mixing rates conform to a basic pattern. The regions above smooth sloping bathymetry are characterized by weak mixing levels with turbulent buoyancy diffusivities of $\kappa \sim 0.1 \times 10^{-4}$ m^2 s^{-1}, while mixing levels and diffusivities above the rough topography of the MAR and its FZs are larger by several orders of magnitude. Here, we present a parameterization of mixing rates based on topographic roughness. In the absence of more extensive dissipation observations, these calculations aim to quantify the role of rough topography in enhancing turbulent mixing rates throughout the Brazil Basin.

1) BATHYMETRIC ROUGHNESS

The seafloor topography data described by Smith and Sandwell (1997, hereafter SS) were used in this study. Smith and Sandwell have used satellite altimetry measurements of the marine gravity field to derive a high-resolution grid of ocean bottom depth. Though they report data at 2-arc-minute resolution, they describe that the transfer from gravity anomaly to topography retains accurate spatial information only on scales greater than ($2\pi \times$ depth), roughly 15 to 25 km in the region near the Mid-Atlantic Ridge. The SS data were used to calculate bathymetric roughness in a series of 0.5° latitude by 0.5° longitude nonoverlapping cells. A roughness parameter z' was calculated as the root-mean-square residual between the SS depth data z and a smoothed field of bathymetry calculated as the polynomial fit $\tilde{z} = a_2x^2 + a_1x + \alpha xy + b_1y + b_2y^2 + c$ over the 0.5° × 0.5° cell. Thus, the roughness calculation is given by

$$z' = \overline{[(z - \tilde{z})^2]}^{1/2} \tag{8}$$

and gives a positive value with units of length. Regions with bathymetric slopes that vary on scales comparable to the 50-km cell size are fit well by the parabolic polynomial estimate, and the residual between z and $\tilde{z}$ is small. Thus, the roughness parameter z' provides a measure of roughness on wavelengths between 15 and 50 km.

Figure 9 shows a map of bottom roughness for the region of the Brazil Basin. The roughness parameter z' is shown using a logarithmic axis for values between 10 and 1000 m. Roughness parameter values of $z' >$ 100 m characterize the region of FZs that extend away from the MAR, and also regions of steep slope in the western part of the basin. These rough regions occupy well over half of the basin's area.

2) PARAMETERIZATION FOR MIXING RATES

We use a model that parameterizes mixing levels throughout the basin in terms of the bottom roughness parameter z'. Specifically, a diffusivity level of $\kappa_b = 0.1 \times 10^{-4}$ m^2 s^{-1} is assigned in each 0.5° × 0.5° cell that is classified as smooth, while data described by Ledwell et al. (2000) and St. Laurent et al. (2001) are used to specify turbulent mixing rates for regions where the topography is classified as rough. The smooth sloping regions where Polzin et al. (1997) observed weak mixing are distinguished by roughness values of $z' \sim O(30$ m), while FZ topography is distinguished by roughness values $z' \sim O(300$ m). Guided by these values, we choose to classify regions with $z' < 100$ m as smooth topography and regions with $z' > 100$ m as rough topography. Profiles of turbulent kinetic energy dissipation rate ϵ are specified as functions of height above the bottom, with separate profiles for bathymetric crests, canyons, and slopes (Fig. 10). Each profile is characterized by dissipation rates that decrease with height. However, the dissipation rates along bathymetric slopes are larger than the dissipation rates along bathymetric crests and canyons. All profiles are characterized by a background value of dissipation rate $\epsilon \simeq 1 \times 10^{-10}$ W kg^{-1} at heights greater than 1 km.

Maps of extrapolated ϵ were produced on four neutral density surfaces (γ = 28.27, 28.205, 28.16, and 28.133 kg m^{-3}) in the following manner. In rough regions, dissipation on each γ surface was assigned the modeled profile value of ϵ at the height of the γ surface above the bottom. Dissipation rates are enhanced where isopycnal surfaces are in close proximity to rough topography. In regions of smooth bathymetry, ϵ is assigned a background value of $\epsilon = (0.1 \times 10^{-4}$ m^2 s$^{-1})\Gamma N^2$, where 0.1×10^{-4} m^2 s^{-1} is the adopted background diffusivity level, $\Gamma = 0.20 \pm 0.04$ is the mixing efficiency ratio (St. Laurent and Schmitt 1999), and the Brunt–Väisälä frequency, N^2, is taken from the isopycnal maps of buoyancy gradient. For each neutral density surface, an average value of turbulent diffusivity is computed from the averaged dissipation rate

$$\overline{\kappa_b} = \Gamma \frac{\overline{\epsilon}}{\overline{N^2}}, \tag{9}$$

where the overbar denotes the average value over the mapped isopycnal surface. Osborn (1980) describes the numerous assumptions underlying the above relationship between dissipation and diffusivity. The uncertainty in the diffusivity estimate is given by

$$\delta\overline{\kappa_b} = \overline{\kappa_b}\left[\left(\frac{\delta\Gamma}{\Gamma}\right)^2 + \left(\frac{\overline{\delta\epsilon}}{\overline{\epsilon}}\right)^2 + \left(\frac{\overline{\delta N^2}}{\overline{N^2}}\right)^2\right]^{1/2}, \tag{10}$$

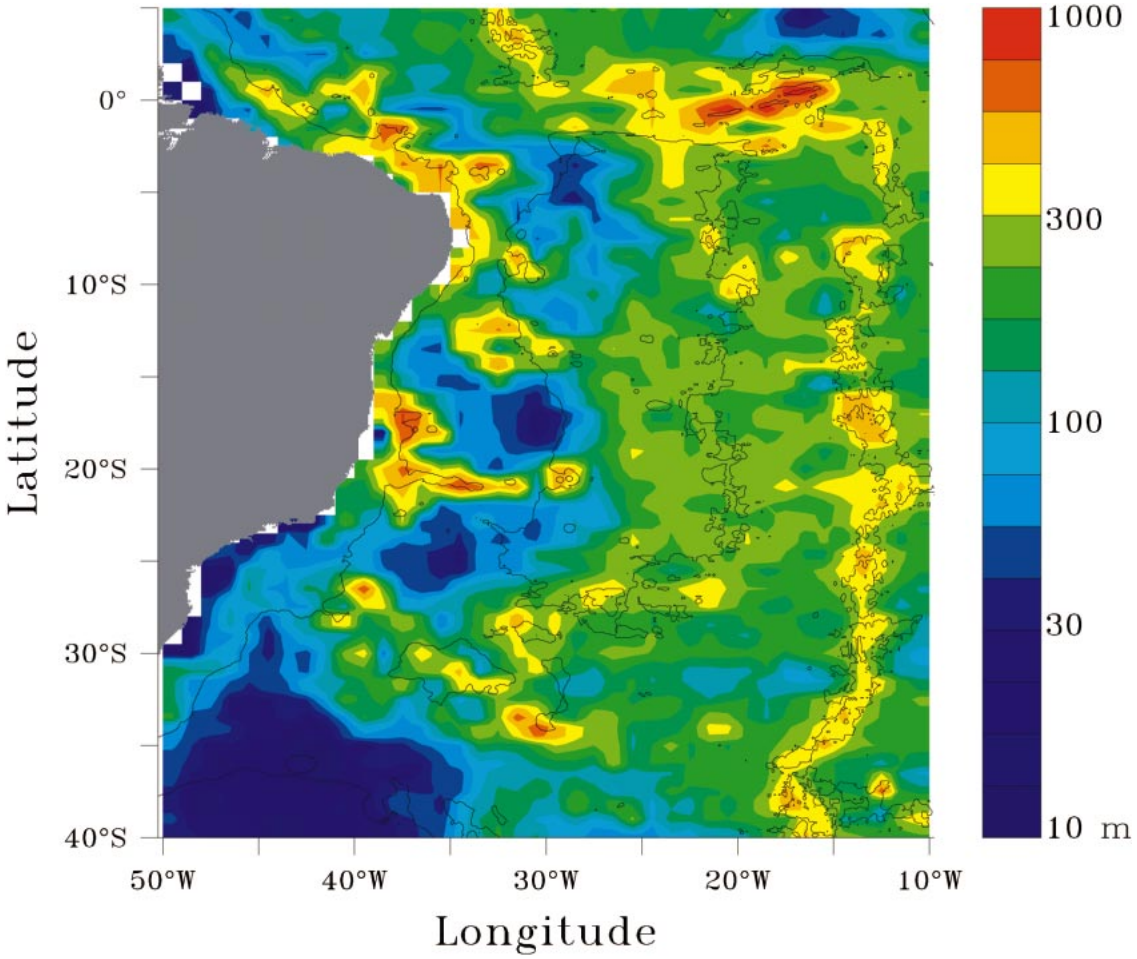

FIG. 9. Bathymetric roughness computed from Smith and Sandwell (1997) topography data. The roughness parameter z' is the vertical scale describing topographic features that deviate from a smooth parabolic representation to the local bathymetry, as calculated in 0.5° × 0.5° nonoverlapping cells. A log scale between 10 and 1000 is used. Contours for the 3000-m and 5000-m isobaths are also shown. The 3000-m isobath of the MAR lies along 15°W longitude. Roughness values with $z' >$ 100 m characterize the region of fracture zones that extend away from the MAR, and also regions of steep slope in the western part of the basin.

where the standard error $\overline{\delta N^2}$ was derived from the objectively mapped hydrography and $\overline{\delta\epsilon}$ accounts for the statistical variability inherent in dissipation rate data, as measured by Brazil Basin microstructure data (St. Laurent et al. 2001).

3. Results

a. Heat balance

The results of the heat budget calculation are discussed first. This repeats an earlier calculation by Hogg et al. (1982); however the κ estimates should be more robust owing to the increased hydrographic data coverage within the basin and the well-measured inflows and outflows at the perimeter of the basin. The Vema Channel is the only open passage into the basin for the volume bounded by $\theta = 0$°C. Heat budget results for this layer are presented in Fig. 5. There are 2.36 Sv of water colder than $\theta = 0$°C entering the Brazil Basin. As water of this temperature does not exit the basin, there must be a volume transport of equal magnitude through the interface bounding the volume to conserve mass. The average upwelling rate across the $\theta = 0$°C surface is $(5 \pm 2) \times 10^{-6}$ m s^{-1}, a factor of 2 lower than Hogg et al.'s (1982) estimate because our $\theta = 0$°C surface area estimate is nearly double the earlier value. As discussed in section 2a, temporal changes in spatial extent are expected to be small; we therefore believe that the original surface area was underestimated due to poor hydrographic data resolution. The basin-averaged vertical diffusivity inferred from the heat budget is $(5.1 \pm 3.0) \times 10^{-4}$ m^2 s^{-1}, equal within uncertainty to Hogg et al.'s previous estimate of 4×10^{-4} m^2 s^{-1}. Similarly, the averaged diffusive heat flux across the $\theta = 0$°C surface, at (3 ± 1) W m^{-2}, is equal within uncertainty to Hogg et al.'s earlier estimate of 3.8 W m^{-2}. The three sources of error for $\overline{\kappa}$ are split more or less equally between

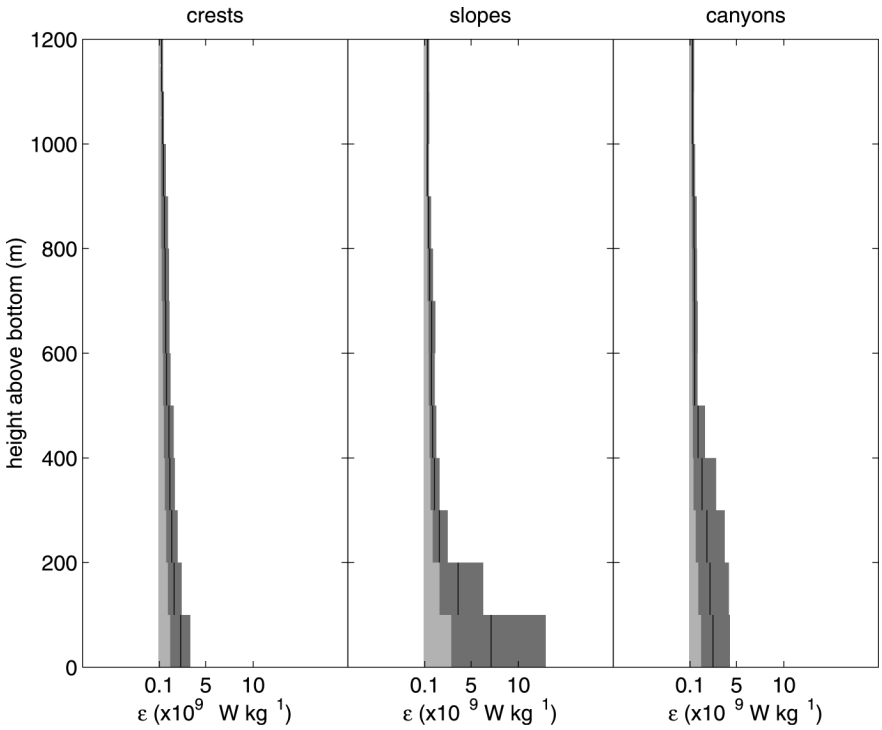

FIG. 10. Averaged profiles of turbulent kinetic energy dissipation rate epsilon from the Brazil Basin. The profiles show 100-m interval depth averages, with the 95% confidence intervals (dark gray shading) about the mean estimates (line segments). The left edge of the light gray shading is at 1×10^{-10} W kg^{-1}.

the uncertainties in the spatial extent of the layer, the area-averaged θ_z and the transports through the Vema Channel. This is our first estimate for $\overline{\kappa}$.

If mixing is carried out by turbulent processes such as shear instability and internal wave-breaking, then inferred diffusivities should be insensitive to whether salt or potential temperature is used in the large-scale tracer budgets. An alternative estimate of $\overline{\kappa}$ is available from the salt budget across the $\theta = 0$°C surface. The calculation is the same as for the heat budget, except that it is necessary to assume a certain spatial distribution for the upwelling. This assumption was not required for the heat budget as θ is uniform on the bounding surface. Assuming that the vertical velocity is uniform on the 0°C surface gives a salt divergence across the volume of 2.36 Sv $\times$ (34.6845 $-$ 34.676) psu $=$ 0.020 psu Sv, where 34.676 psu is the transport-weighted salinity at the Vema Channel and 34.6845 psu is the average salinity value over the 0°C surface estimated from the hydrographic climatology. A diffusive salt flux of 0.020 psu Sv across the $\theta = 0$°C surface is required to maintain a steady-state balance. The averaged vertical salinity gradient across the 0°C surface is 9.73×10^{-5} psu m^{-1}. This yields a mixing coefficient $\overline{\kappa_{\text{salt}}} \sim 4.6 \times 10^{-4}$ m^2 s^{-1}, which is in encouraging agreement with our first more accurate estimate based on heat conservation.

TABLE 3a. The results of the heat budget calculation. The averaged upwelling rates and diffusive heat fluxes over the four bounding θ surfaces are given in the second and third columns. Vertical diffusivity coefficients averaged over the θ surfaces, $\overline{\kappa_\theta}$, are given in the last column.

θ surface (°C)	Upwelling rates ($\times 10^{-7}$ m s^{-1})	Diffusive heat flux (W m^{-2})	$\overline{\kappa_\theta}$ ($\times 10^{-4}$ m^2 s^{-1})
1.6	5 ± 4	3.0 ± 2.1	3.3 ± 2.4
1.2	5 ± 3	2.6 ± 1.5	3.0 ± 1.8
0.8	7 ± 3	2.3 ± 1.1	3.3 ± 1.6
0	52 ± 21	2.7 ± 1.1	5.1 ± 3.0

Heat budget results for the three more buoyant layers are displayed in Figs. 6–8. Inflows and outflows to the basin are no longer restricted to the Vema Channel, and the relative contribution to advective fluxes at each passage is also shown. The major source of uncertainty for κ is due to the combined error in the directly measured fluxes, particularly those associated with the inflow through the Vema Channel. Averaged upwelling rates, heat fluxes, and inferred diffusivites for all surfaces are summarized in Table 3a. Diffusivity estimates are the least certain of the three as they hinge on assumptions relating turbulent transports to large-scale fluxes. Upwelling rates and associated heat fluxes within the AABW volume range between 0.5 and 5($\times 10^{-6}$ m s^{-1}) and 2 and 3 W m^{-2}. These values are fairly typical for abyssal plains in the South Atlantic or any of the major ocean basins (e.g., McCarthy et al. 1997, for a recent review). Correspondingly, the estimated diffusivity val-

TABLE 3b. The results of the density budget calculations, as well as mixing rate results from the parameterized bathymetric roughness computation. Upwelling rates and diffusivity coefficients, $\overline{\kappa_\gamma}$, from the density budget calculation are given in the second and third columns. Dissipation, $\overline{\epsilon}$, and diffusivity coefficients, $\overline{\kappa_b}$, from the parameterized bathymetric roughness model are shown in the two right-hand columns. All properties are averaged over the four neutral density surfaces.

γ surface (kg m^{-3})	Upwelling rates ($\times 10^{-7}$ m s^{-1})	$\overline{\kappa_\gamma}$ ($\times 10^{-4}$ m^2 s^{-1})	$\overline{\epsilon}$ ($\times 10^{-9}$ W kg^{-1})	$\overline{\kappa_b}$ ($\times 10^{-4}$ m^2 s^{-1})
28.133	4 ± 4	2.9 ± 2.3	1.2 ± 0.38	1.2 ± 0.6
28.160	4 ± 3	2.0 ± 1.3	1.3 ± 0.40	1.2 ± 0.6
28.205	6 ± 3	1.8 ± 0.8	1.6 ± 0.49	1.8 ± 1.1
28.270	11 ± 4	1.8 ± 0.8	2.1 ± 0.67	3.1 ± 1.8

ues, which are equal within error bars for all four surfaces, $\kappa \sim 3$–$5(\times 10^{-4}$ m^2 s$^{-1})$, fall within the range of previous estimates based on heat budgets.

Cross-isotherm motions associated with turbulent transports are not spread uniformly across all surfaces lying within the AABW. The total amount of water advected through the coldest surface is equal within a factor of 2 to the amount upwelled through the more buoyant layers in the AABW. This implies upwelling rates that are an order of magnitude higher for the coldest surface since the spatial extent of the coldest θ surface is a small fraction ($\sim$1/10) of the shallower surfaces. Proximity of the cold surface to the ocean bottom may help explain the elevated vertical velocities that are observed. No vertical structure in vertical velocity is apparent higher up in the AABW layer, where upwelling rates at the representative surfaces are equal within uncertainty. Interestingly, the large vertical transports associated with the deepest surface do not translate to stronger diffusive heat fluxes and increased levels of mixing. A weaker mean vertical temperature gradient offsets the larger vertical velocities, with the result that the averaged diffusive heat fluxes through any surface in the AABW layer are more or less equal.

b. Density budget: Importance of lateral mixing

One of the purposes of this study is to determine whether diffusivity estimates based on the scalar conservation equation (2) are biased high due to lateral mixing effects. We gain insight into the significance of lateral fluxes by comparing diffusivities inferred from heat and density budgets. The calculations of the previous section are repeated but neutral density replaces potential temperature as the tracer. Results are summarized in Table 3b. Averaged vertical velocities deduced from the density budgets do not intensify with depth as strongly as they did for the heat budget analysis. In fact, upwelling rates are uniform across all γ surfaces within estimation uncertainty. This is consistent with isopycnal transports contributing significantly to the upwelling estimate across the $\theta = 0$°C surface.

However, there is no discernible difference in mixing rates throughout the AABW layer; $\overline{\kappa_\gamma}$ is around 2×10^{-4} m^2 s^{-1} for each surface. More importantly, turbulent mixing coeffients $\overline{\kappa_\gamma}$ are also equal within uncertainty to those deduced from the heat budget analysis, i.e., $\overline{\kappa_\theta} = 3 - 5 \times 10^{-4}$ m^2 s^{-1}, implying that lateral fluxes do not make an important contribution to the turbulent flux across isotherms. Perhaps we should qualify this by saying that we are presently unable to detect any contribution that lateral fluxes might make given the disappointingly large estimation errors. We do see a systematic reduction in $\overline{\kappa_\gamma}$ with respect to $\overline{\kappa_\theta}$ although this is not significant within uncertainty bounds.

c. Mixing rates from parameterized bathymetric roughness

The averaged mixing and dissipation rates on neutral surfaces calculated using the bottom roughness parameterization described in section 2c are shown in Table 3b. The surface-averaged dissipation $\overline{\epsilon}$ and diffusivities $\overline{\kappa_b}$ at the four different surfaces are indistinguishable at the level of one standard error. The four $\overline{\kappa_b}$ estimates are also equal within uncertainty levels to the density budget derived $\overline{\kappa_\gamma}$ estimates shown in Table 3b. As in the case of the density budget derived $\overline{\kappa_\gamma}$ estimates, large uncertainty estimates obscure differences in diffusivity estimates at different depths.

SENSITIVITY OF ROUGHNESS PARAMETERIZATION

The dissipation-based mixing rates were calculated using a specification that designates rough bathymetry as having $z' > 100$ m. While the value of $z' = 100$ m is a subjective partition between rough and smooth classes of topography, histograms of the parameter z' for the regions bounded by the $\gamma = 28.27$, 28.205, 28.16, and 28.133 kg m^{-3} density surfaces suggest that there is merit to this classification scheme. As shown for the case of the region bounded by $\gamma = 28.27$ in Fig. 11, the statistical distribution of the roughness parameter z' is bimodal with an antimode close to $z' \sim 100$ m. All four surfaces include the region bounded by the $\gamma = 28.27$ surface, and all four surfaces have bimodal roughness statistics. Because $z' \sim 100$ m corresponds to an antimode in the statistical distribution of z', the calculations for mixing rates are rather insensitive to the precise value of z' used to partition smooth from rough bathymetry. For example, for the $\gamma = 28.27$ kg m^{-3} surface, the best estimate of $\overline{\kappa_b}$ becomes $\overline{\kappa_b} = 4.4 \times$

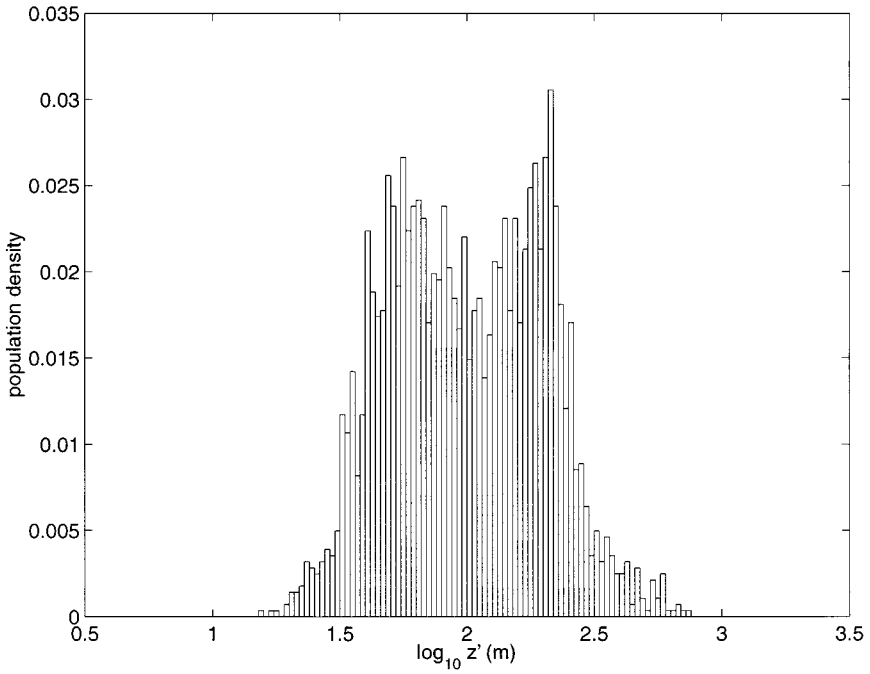

FIG. 11. Histogram of roughness parameter z' for the region bounded by the $\gamma = 28.27$ kg m^{-3} neutral density surface. The statistical distribution is bimodal, with an antimode near $z' \sim 100$ m. The z' statistical distributions for the regions bounded by $\gamma = 28.205$, 28.16, and 28.133 are also bimodal about an antimode near $z' \sim 100$ m.

10^{-4} m^2 s^{-1} if $z' = 50$ m is used to distinguish smooth from rough regions, while $\overline{\kappa_b} = 2.3 \times 10^{-4}$ m^2 s^{-1} if $z' = 150$ m is used. Both of these $\overline{\kappa_b}$ estimates fall within one standard error of the $z' = 100$ m estimate.

4. Discussion and summary

It is worth considering whether there are any other significant neglected terms in the underlying equations used to infer $\overline{\kappa_\gamma}$ and $\overline{\kappa_\theta}$. We are interested in terms that may have been ignored in the budgets but are of comparable size to the turbulent flux divergences $(\kappa\theta_z)_z$ and $(\kappa\gamma_z)_z$.

a. Steady-state balance

The steady-state assumption is common to both approaches. In order to demonstrate its validity we need to show that the time-dependent terms neglected in (2) are small compared to those that have been retained. In particular, the problem is to estimate the size of $\langle \int_V \theta_t \, dV \rangle$, where the angle brackets refer to a time average over a period τ and show that this term is small compared to $\langle \nabla \cdot (\mathbf{u}\theta) \rangle$ and $\langle \kappa\theta_{zz} \rangle$. Note that any time-dependence arising in the volume-integrated heat equation must be due to the boundary conditions, that is, changes of the fluxes in and out of the basin or changes at the upper interface due to the overlying North Atlantic Deep Water. Writing the time-dependent balance:

$$\int_V \theta_t \, dV + \int_A (\mathbf{u}\theta) \cdot \mathbf{n} \, dA = \int_V \kappa\theta_{zz} \, dV, \quad (11)$$

and letting the individual temperature fluxes $M_i\theta_i$ [defined in (6)] be denoted by h_i gives

$$\int_V \theta_t \, dV + h_{\text{Vema}} + h_{\text{Hunter}} + h_{36\text{W}} + h_{\text{RFZ/CFZ}} + h_{\text{upw}} = \int_V \kappa\theta_{zz} \, dV. \quad (12)$$

Significant time variability has been observed at the moored arrays and from hydrographic data in the terms contributing to h_i, at timescales varying from high frequency (weeks), to annual, to long term drift (decades). This variability occurs in both mass transports and temperatures. The issue is: how do these changes in h_i affect the time-dependent balance (and in particular the $\langle \nabla \cdot (\mathbf{u}\theta) \rangle$ term)? While this is clearly a very complicated question, beyond the scope of this paper to answer in detail, it is nevertheless possible to estimate the impact of time-dependence in several simple scenarios.

First, we recognize that we have obtained (2) by averaging over periods of years, so high-frequency changes will have little effect on our calculation. Instead we concern ourselves with the long-term variability. Ideally we would like estimates of θ_t over the volume for the averaging interval τ. Since we do not have sufficient

observations to measure $\langle \int_V \theta_t \, dV \rangle$ directly, we need to infer it from observed changes in the fluxes at the inflows and outflows. There is a mismatch in τ for the various terms: fluxes at the inflows and outflows have been averaged over a period of a few years; layer boundaries and curvatures have been averaged over periods of decades.

Long-term trends in both bottom water temperature and in total transport of AABW were observed at the Vema Channel (Hogg and Zenk 1997), so we use these numbers for our simple examples. The observed increase in temperature of the deepest water of the Vema inflow was 0.03°C, and it occurred over a period of about 2 years. Suppose that all the water below 0.8°C increased on average by this amount but that the volume transport was unchanged. Assuming that all other processes in (12) remained constant, the reservoir of water below 0.8°C in the Brazil Basin would warm at a rate of only $\sim$0.001°C yr^{-1} corresponding to a volume-integrated value $\langle \int_V \theta_t \, dV \rangle = 0.12$°C Sv. While this number is comparable to some of the terms in the balance for this layer (see Fig. 6), it is only 4% the size of the upwelled temperature flux, which dominates the balance, and hence it is small compared to the volume-averaged downward diffusion value of 2.96°C Sv (or 0.025°C yr^{-1}). On the other hand, the effect in the layer colder than 0°C would be more pronounced because this volume is so much smaller: warming would occur at a rate of 0.055°C yr^{-1}, equivalent to a volume-integrated value of 0.07°C Sv, compared to 0.3°C Sv for the downward diffusion, or roughly 24%.

A change in mass flux entering or exiting the basin would affect not only the heat balance within the basin but the mass balance as well, which our basic analysis also assumes to be in steady state. Hogg and Zenk (1997) reported a decrease in the strength of the Vema Channel velocities during 1991–92 at the rate of 5 cm s^{-1} over 1000 days, or around 20% over a 3-yr period. For our purposes, consider the effect of an abrupt, 1 Sv decrease in the Vema inflow below $\theta = 0.8$°C (about 25%): such a decrease corresponds to a yearly change in the volume of water colder than 0.8°C of less than 1%, or a change of 5% over 6 years. The corresponding decrease in area would be $\sim$2% or less for this layer. After what would probably be a relatively long adjustment period (let us suppose 10 years), and in the absence of additional changes, a new equilibrium would be attained. Consider two extreme cases.

Case 1. Most of the mass flux change is compensated by a shutoff of the equatorial flow, and the rest by reduced upwelling. The net heat divergence in this scenario would be 2.43°C Sv, which would represent a decrease of about 22% from the previous equilibrium. If we assume that the turbulent fluxes are determined by other dynamics, then to achieve a balance would require a reduction in the vertical temperature gradient of about 20%. Physically, what is happening? As the new mass fluxes come into balance, at first more heat diffuses downward than necessary to achieve equilibrium in the heat balance (because the vertical temperature gradient is as yet unchanged). Hence the volume begins to warm, which corresponds to a lowering of the upper surface and decreasing layer volume. Moreover, warming should lead to reduced overall difference in the temperature extremes in the volume: that is, reduced vertical temperature gradients.

Case 2. The mass flux change is completely compensated by a reduction in upwelling. In this case, the horizontal convergence would be nearly unchanged but the upwelled heat flux would be decreased. The net heat divergence would be 2.35°C Sv, not much different than in Case 1 and with a similar reduction in the vertical temperature gradient. The reason both of these scenarios lead to similar results is that the temperature of the mass fluxes leaving at the equator is nearly equal to the temperature of the interface. For the 1.6°C surface, the difference would be greater: compensation at the equator would require about a 13% reduction in θ_z, compared to compensation entirely by upwelling, with a 25% reduction in θ_z.

b. Nonlinearities in equation of state

Density budgets are complicated by density production terms due to nonlinearities in the equation of state (McDougall 1987; Davis 1994). It is relatively straightforward to estimate the size of various neglected terms for our situation using published formulas (e.g., McDougall 1987; Davis 1994) and our maps of hydrographic properties. For instance, the density source due to lateral fluxes interacting with nonlinearities in the equation of state requires basinwide estimates of horizontal gradients in θ and salinity. We find that the surface-averaged density changes due to interaction between mixing and nonlinearities in the equation of state (which includes thermobaricity and cabbeling) are of order 10^{-14} to 10^{-13} kg m^{-3} s^{-1} for assumed lateral diffusivities of $K_H = O(100)$ m^2 s^{-1} and vertical diffusivities $\kappa = O(10^{-5} - 10^{-4})$ m^2 s^{-1}. These are small relative to the volume-averaged divergence of turbulent density flux $(\kappa\gamma_z)_z$ and the term $\kappa\gamma_{zz} = O(5 \times 10^{-12})$ kg m^{-3} s^{-1} if $\kappa = O(10^{-5})$ m^2 s^{-1}. The result is inconclusive as the relative size of the neglected terms depends on assumed values of lateral and diapycnal diffusivities (e.g., McDougall 1987; Davis 1994). If our estimate of the intensity of diapycnal mixing is correct at $\kappa = O(10^{-4})$ m^2 s^{-1}, then we are justified in neglecting density production due to interactions between mixing and equation of state nonlinearities. If the real level of diffusive mixing is an order of magnitude weaker, then the situation is much more complicated. In that

scenario, we would have incorrectly represented some possibly large fraction of the observed residual term $\nabla\cdot(\gamma\mathbf{u}) = O[0.5\text{–}1\ (\times 10^{-10}\ \text{kg m}^{-3}\ \text{s}^{-1})]$ as a divergence in density flux whose true value may be closer to $O(10^{-11})$ kg m^{-3} s^{-1} or smaller (the size is difficult to estimate as $\kappa_z\gamma_z$ may be large on deeper surfaces). It is unlikely that these density production terms alone can make up a shortfall of $O(10^{-11}\ \text{kg m}^{-3}\ \text{s}^{-1})$ to balance the residual term. On the other hand, it is not inconceivable that some combination of these terms along with low-frequency variability could dominate a relatively weak density flux divergence.

c. Summary

Diffusive heat fluxes and turbulent diffusivities inferred from heat and large-scale budget considerations are indistinguishable within error bars for four surfaces within the AABW layer. Mixing coefficients inferred from heat budgets fall in the range $\overline{\kappa_\theta} \sim 3\text{–}5(\times 10^{-4}$ m^2 s^{-1}). Our estimates agree within error with those of Hogg et al. (1982), $\overline{\kappa_\theta} \sim 3\text{–}4(\times 10^{-4}$ m^2 s^{-1}), but are more robust owing to increased data coverage within the basin interior and at the deep passages. The agreement between $\overline{\kappa_\theta}$ and the mixing rates inferred from density budgets ($\overline{\kappa_\gamma} \sim 2 \times 10^{-4}$ m^2 s^{-1}) implies that lateral eddy fluxes of heat along isopycnals do not contribute significantly to the heat flux, although estimates of $\overline{\kappa_\gamma}$ are consistently lower than those for $\overline{\kappa_\theta}$. This conclusion agrees with findings from a previous study by McDougall and Whitehead (1984) who also estimated the relative importance of mixing processes in modifying Antarctic Bottom Water. Using a different methodology and studying transformation processes mainly in the North Atlantic, they found that diapycnal mixing dominated lateral mixing in the heat budget, which they found to be insignificant.

The model estimates based on bathymetric roughness provide independent confirmation of the diapycnal mixing rates calculated by inference from large-scale budgets. Observations of tracer dispersion and microstructure from the Brazil Basin Tracer Release Experiment (Ledwell et al. 2000; Polzin et al. 1997) suggest that diapycnal mixing is strongly enhanced in regions of rough bathymetry to levels far greater than those observed over smooth abyssal plains. The results from that experiment provided the motivation to investigate the role of bottom roughness on mixing rates over the entire Brazil Basin. A parameterization of the vertical profile of dissipation as a function of bathymetric roughness was used to obtain dissipation estimates on neutral surfaces (St. Laurent et al. 2001). The dissipation estimates were related to turbulent diffusivity to yield basin-averaged estimates $\overline{\kappa_b} \sim 1\text{–}3(\times 10^{-4}\,\text{m}^2\,\text{s}^{-1})$ in agreement with the heat and density budget mixing rates within experimental uncertainty.

Acknowledgments. We thank W. Smethie, Jr. (LDEO), G. Siedler, T. Muller, and W. Zenk (all at the Institut für Meereskunde, Kiel), and H. Mercier and M. Arhan (both at IFREMER Centre de Brest) for the early release of their WOCE CTD data. We also thank H. Mercier and K. Speer (The Florida State University) for sharing current meter and CTD data from the Romanche and Chain Fracture Zones with us. This research was supported by Devonshire Associates, through a WHOI fellowship, W. Van Alan Clark Jr., and the Division of Ocean Sciences, National Science Foundation under Grants OCE 98-18266, OCE 94-15589, and OCE 99-11148. This work was significantly improved by comments from W. Owens, R. Huang, J. Toole, and two anonymous reviewers.

APPENDIX A

Temperature Interpolation

As mentioned in the text, only at the 36°W array location is the vertical temperature profile other than simply linear. In particular, the structure is piecewise linear in three segments throughout the AABW and North Atlantic Deep Water (see Hall et al. 1997, their Fig. 7), with the breaks in slope occurring at about $\theta = 0.86$°C and $\theta = 1.91$°C. Only the two coldest segments are relevant to the calculations in this paper, but all three are necessary for the prediction scheme interpolating temperature to obtain time series of the 0.8°, 1.2°, and 1.6°C isotherm depths. The average slope of the temperature profile in each of the three segments has been determined from the 22 CTD profiles collected during deployment and recovery: those slopes are 1.10×10^{-3}, 3.69×10^{-3}, and 5.72×10^{-4} °C m^{-1} in the coldest, middle, and warmest segments respectively.

Temperature time series were obtained at 3900, 4100, and 4300 m for all six moorings. The temperature prediction scheme looks at which part of the gradient each measurement lies in. Linear interpolation between two measurements is used when both lie in the same linear portion; otherwise the average slopes are used as a guide to establish a three-part linear profile consistent with the measured temperatures. This profile is not constrained to reproduce the measured temperatures exactly in most cases, so an estimate of the error in the prediction scheme is obtained by comparing the predicted temperatures with the actual ones. The rms differences between predicted and actual temperatures for all six moorings are 0.0234°, 0.0477°, and 0.0310°C for the 3900, 4100, and 4300 m levels, respectively. The rms difference over all depths and moorings is 0.0355°C or ~0.04°C. Because the error is expected to be largest at the 36°W location, we consider 0.04°C to be an upper bound on the temperature interpolation error, and use this in the error calculation described in the text.

APPENDIX B

Individual Error Terms

The errors in mass transports for each location comprise the following specific temporal and spatial sampling errors. The term ''temporal sampling error'' here refers to the standard error of the mean. The term ''spatial errors'' subsumes all other errors incurred in making the transport estimates.

a. Vema Channel

The fluxes were calculated using a somewhat different method than at the remaining channels so the error estimation also differs. In essence, the mean fluxes have been estimated from one realization of the field, so the errors have been broken into two parts: the so-called ''baroclinic'' errors, which come from trying to estimate a mean from a synoptic section (using the moored measurements to estimate the eddy noise), and the so-called ''barotropic'' errors, which come from trying to determine the reference level from the moored array. Without going into detail, we note that it turns out that the temperature flux errors are in proportion to the mass flux errors (i.e., for a mass flux error of 30%, e.g., there is a temperature flux error of 30%). Furthermore, except in the coldest layer, the baroclinic error dominates by a factor of 1.1–1.6 times the barotropic error.

b. Hunter Channel

All errors were estimated from the discussion of Zenk et al. (1999, p. 2798). The temporal error is quoted as 40% of the total transport, which we assume is distributed evenly with depth. Zenk et al. (1999) quote an error of the net AABW transport estimated from changing the upper boundary of the AABW but, since this occurs above all the layers under consideration here, it does not affect the overall error. On the other hand, using a different boundary layer profile at the bottom results in an error of 0.1 Sv, which affects all layers. Uncertainty about the horizontal extrapolation scheme used to integrate the transport results in a net 0.3 Sv error, distributed evenly in the vertical, compared to the total transport of 2.92 Sv, or 10%. A final error (resulting from a complicated vertical interpolation scheme where one instrument failed) is estimated to be 0.23 Sv, or 8% of the mean, which we again assume is evenly distributed over depth. All of these errors are assumed to be independent.

c. Romanche and Chain Fracture Zones (RFZ/CFZ)

Errors in the transport estimates for these two locations (lumped as one number in the tables) were much smaller than at other locations because 1) the layer transports themselves were smaller and 2) their standard errors were on the order of just 5% of the means, compared to 12%–15% for 36°W and 40% for the Hunter Channel. This difference is due rather to proportionally smaller standard deviations than significantly more degrees of freedom. Integral timescales varied from layer to layer: the degrees of freedom for each layer were (26, 74, 51) for the RFZ for $\theta = (0.8, 1.2, 1.6)$°C respectively, and (11, 97, 94) for the CFZ for the same layers. Mercier and Speer (1998) cited spatial sampling errors of 10%–15% of the mean; we conservatively used 15% to estimate our total errors.

d. Equatorial passage at 36°W

The integral timescales were estimated directly from time series of the transport for the various layers, and are 7–7.5 days, leading to 40–43 degrees of freedom for the 604-day-long time series. Two major spatial sampling errors are considered. The first is due to possible undersampling of the flow in the near-bottom water: Based on measured near-bottom shear at the equatorial mooring, a depth of 150 m, and a width of the AABW flow of 200 km we estimate an error of $0.7 \text{ cm s}^{-1} \times 150 \text{ m} \times 200 \text{ km} = 0.21$ Sv for all layers. The other possible error is due to anomalously low flow at the 1°S mooring, which may have been in the lee of a bump: assuming the velocity should have been more like that at the moorings to north and south, the transport would increase by 0.3 Sv over the total of 2.0 Sv, or 15%, evenly distributed with depth.

REFERENCES

Curry, R., 1996: HydroBase: A database of hydrographic stations and tools for climatological analysis. Woods Hole Oceanographic Institution Tech. Rep. WHOI-96-01, 50 pp. [Available from Woods Hole Oceanographic Institution, Woods Hole, MA 02543.]

Davis, R., 1994: Diapycnal mixing in the ocean: Equations for large-scale budgets. *J. Phys. Oceanogr.*, **24,** 777–800.

——, 1998: Preliminary results from directly measuring middepth circulation in the tropical and South Pacific. *J. Geophys. Res.*, **103,** 24 619–24 639.

Hall, M. M., M. McCartney, and J. A. Whitehead, 1997: Antarctic Bottom Water flux in the equatorial western Atlantic. *J. Phys. Oceanogr.*, **27,** 1903–1927.

Hogg, N., and W. Zenk, 1997: Long-period changes in the bottom water flowing through the Vema Channel. *J. Geophys. Res.*, **102,** 15 639–15 646.

——, P. Biscaye, W. Gardner, and W. Schmitz Jr., 1982: On the transport and modification of Antarctic Bottom Water in the Vema Channel. *J. Mar. Res.*, **40** (Suppl.), 231–263.

——, W. Owens, G. Siedler, and W. Zenk, 1996: Circulation in the Deep Brazil Basin. *The South Atlantic, Present and Past Circulation*, G. Wefer et al., Eds., Springer, 249–260.

——, G. Siedler, and W. Zenk, 1999: Circulation and variability at the southern boundary of the Brazil Basin. *J. Phys. Oceanogr.*, **29,** 145–157.

Jackett, D. R., and T. J. McDougall, 1997: A neutral density variable for the world's oceans. *J. Phys. Oceanogr.*, **27,** 237–263.

Ledwell, J., E. Montgomery, K. Polzin, L. St. Laurent, R. Schmitt, and J. Toole, 2000: Evidence for enhanced mixing over rough topography in the abyssal ocean. *Nature*, **403,** 179–182.

Lueck, R., and T. Mudge, 1997: Topographically induced mixing around a shallow seamount. *Science,* **276,** 1831–1833.

McCarthy, M., L. Talley, and M. Baringer, 1997: Deep upwelling and diffusivity in the southern Central Indian Basin. *Geophys. Res. Lett.,* **24,** 2801–2804.

McDougall, T., 1987: Thermobaricity, cabelling and water-mass conversion. *J. Geophys. Res.,* **92,** 5448–5464.

——, and J. Whitehead, 1984: Estimates of the relative roles of diapycnal, isopycnal and double-diffusive mixing in Antarctic Bottom Water in the North Atlantic. *J. Geophys. Res.*, **89,** 10 479–10 483.

Memery, L., M. Arhan, X. Alvarez-Salgado, M.-J. Messias, H. Mercier, C. Castro, and A. Rios, 2000: The water masses along the western boundary of the South and Equatorial Atlantic. *Progress in Oceanography,* Vol. 47, Pergamon, 69–98.

Mercier, H., and K. Speer, 1998: Transport of bottom water in the Romanche Fracture Zone and the Chain Fracture Zone. *J. Phys. Oceanogr.,* **28,** 779–790.

Munk, W., 1966: Abyssal recipes. *Deep-Sea Res.*, **13,** 707–730.

Osborn, T., 1980: Estimates of the local rate of vertical diffusion from dissipation measurements. *J. Phys. Oceanogr.,* **10,** 83–89.

Polzin, K., J. Toole, J. Ledwell, and R. Schmitt, 1997: Spatial variability of turbulent mixing in the Abyssal Ocean. *Science,* **276,** 93–96.

Reid, J., 1989: On the total geostrophic circulation of the South Atlantic Ocean: Flow patterns, tracers and transports. *Progress in Oceanography,* Vol. 23, Pergamon, 149–244.

Smith, W., and D. Sandwell, 1997: Global sea floor topography from satellite altimetry and ship depth soundings. *Science,* **277,** 1956–1962.

St. Laurent, L., and R. Schmitt, 1999: The contribution of salt fingers to the North Atlantic Tracer Release Experiment. *J. Phys. Oceanogr.,* **29,** 1404–1424.

——, J. Toole, and R. Schmitt, 2001: Buoyancy forcing by turbulence above rough topography in the abyssal Brazil Basin. *J. Phys. Oceanogr.*, in press.

Stommel, H., 1958: The abyssal circulation. *Deep-Sea Res.,* **5,** 80–82.

Stramma, L., and M. England, 1999: On the water masses and mean circulation of the South Atlantic Ocean. *J. Geophys. Res.,* **104,** 20 863–20 883.

Toole, J., J. Ledwell, K. Polzin, R. Schmitt, E. Montgomery, and L. St. Laurent, 1997a: The Brazil Basin Tracer Release Experiment. International *WOCE Newsletter* No. 28, 39 pp. [Available from the WOCE International Project Office, Southampton Oceanography Centre, Southampton SO14 3ZH, United Kingdom]

——, R. Schmitt, K. Polzin, and E. Kunze, 1997b: Near-boundary mixing above the flanks of a midlatitude seamount. *J. Geophys. Res.*, **102,** 947–959.

Whitehead, J., and L. V. Worthington, 1982: The flux and mixing rates of Antarctic Bottom Water within the North Atlantic. *J. Geophys. Res.*, **87,** 7903–7924.

Zenk, W., G. Siedler, B. Lenz, and N. Hogg, 1999: Antarctic Bottom Water flow through the Hunter Channel. *J. Phys. Oceanogr.*, **29,** 2785–2801.